Front. Optoelectron. 2017, 10(1): 18–30
DOI 10.1007/s12200-017-0702-z

RESEARCH ARTICLE

Characterization of basic physical properties of Sb_2Se_3 and its relevance for photovoltaics

Chao CHEN[1], David C. BOBELA[2], Ye YANG[2], Shuaicheng LU[1], Kai ZENG[1], Cong GE[1], Bo YANG[1], Liang GAO[1], Yang ZHAO[1], Matthew C. BEARD[2], Jiang TANG (✉)[1]

1 Wuhan National Laboratory for Optoelectronics (WNLO), Huazhong University of Science and Technology, Wuhan 430074, China
2 Chemistry and Nanoscience Center, National Renewable Energy Laboratory, Golden, CO, 80401, USA

© Higher Education Press and Springer-Verlag Berlin Heidelberg 2017

Abstract Antimony selenide (Sb_2Se_3) is a promising absorber material for thin film photovoltaics because of its attractive material, optical and electrical properties. In recent years, the power conversion efficiency (PCE) of Sb_2Se_3 thin film solar cells has gradually enhanced to 5.6%. In this article, we systematically studied the basic physical properties of Sb_2Se_3 such as dielectric constant, anisotropic mobility, carrier lifetime, diffusion length, defect depth, defect density and optical band tail states. We believe such a comprehensive characterization of the basic physical properties of Sb_2Se_3 lays a solid foundation for further optimization of solar device performance.

Keywords antimony selenide (Sb_2Se_3), mobility, lifetime, diffusion length, defects

1 Introduction

Antimony selenide (Sb_2Se_3), a semiconductor possessing one dimensional crystal structure [1], is an excellent photovoltaic absorber due to its high absorption coefficient ($>10^5$ cm^{-1}) at visible region [2], 1.17 eV band gap (optimal for single junction solar cells) [3], simple binary composition with fixed orthorhombic phase [4], low toxicity, and earth-abundant constituents. What's more, theoretical calculation and experimental characterizations confirmed that Sb_2Se_3 has benign grain boundaries (GBs) if properly aligned along the ribbon direction [5]. In recent years, through steady improvements in the growth of these aligned Sb_2Se_3 films, power conversion efficiency (PCE) of Sb_2Se_3 thin film solar cells has increased to 5.6% [5–9], which is larger than other non-cubic semiconductor thin film solar cells such as SnS (reported best PCE of 4.6%) [10].

Received January 16, 2017; accepted January 24, 2017

E-mail: jtang@mail.hust.edu.cn

Despite the rapid improvement, the device efficiency is still far behind conventional copper indium gallium selenide (CIGS, PCE = 22.3%) [11], cadmium telluride (CdTe, PCE = 22.1%) [12], copper zinc tin sulfoselenide (CZTSSe, PCE = 12.6%) [13], and even amorphous silicon (PCE = 13.6%) solar cells [14]. One reason is that the fundamental features of thin film Sb_2Se_3 such as mobility, carrier lifetime, diffusion length, defect depth, defect density and optical band tails remain largely unexplored. Only film conductivity and carrier mobilities were reported in few previous studies [15,16]. The study on Sb_2Se_3 is lacking because of three difficulties: the intrinsically low electrical conductivity ($10^{-6}-10^{-7}$ $S\cdot cm^{-1}$) of Sb_2Se_3 film creates obstacles for obtaining carrier density and mobility directly from Hall effect measurement [17]; the absence of photoluminescence due to its indirect bandgap makes us obtain carrier lifetime and defect information challenging; and the strong anisotropy in Sb_2Se_3 crystal renders mobility measurement very complicated. Nevertheless, understanding these fundamental parameters of thin film Sb_2Se_3 is of great importance to device configuration design, performance, and optimization. Given the great potential already demonstrated, further investigation of these properties is thus urgently needed.

In this article, time of fight (TOF) measurement was used to determine the anisotropic mobilities. Time-resolved transient absorption (TA) spectroscopy was used to probe dynamics of photogenerated carriers, and thus determine carrier lifetimes [18]. Minority carrier (electron) diffusion length was directly characterized through biased internal quantum efficiency (IQE) measurement, and was calculated from the mobility-lifetime product as well. Temperature dependent dark conductivity and thermal admittance spectroscopy (TAS) was applied to determine the depth and density of defect states in thin film Sb_2Se_3, respectively. Lastly, photothermal deflection spectroscopy (PDS) was used to probe disorder by measuring optical band tails of crystal Sb_2Se_3 (c-Sb_2Se_3) and amorphous

Sb_2Se_3 (a-Sb_2Se_3) films. A table summarizing all the parameters is included for readers' convenience, followed by the discussion of their relevance for photovoltaic application (Table 1 in Section 4). We believe such a comprehensive characterization of the basic physical properties of Sb_2Se_3 film lays a solid foundation for further optimization of device performance.

2 Experimental section

2.1 Martials preparation

Sb_2Se_3 films were prepared using rapid thermal evaporation (RTE). The procedure details could be found elsewhere [5]. [120]- and [221]-Sb_2Se_3 films were deposited at substrate temperature of 280°C and 300°C, respectively. [020]-Sb_2Se_3 films were prepared at 280°C with the substrates pre-coated with 5 nm amorphous Sb_2Se_3 which was used to induce oriented growth. Sb_2Se_3 film thickness was adjusted by varying the evaporation time. Au electrode was fabricated by thermal evaporationy.

2.2 Sb_2Se_3 solar cells fabrication

Glass/ITO/CdS/Sb_2Se_3/Au devices were used for biased IQE and TAS measurement. The substrate is in-doping tin oxide (ITO)-coated glass. CdS buffer layer was deposited by chemical bath deposition (CBD) with the thickness about 60 nm [5]. Sb_2Se_3 absorption layer and Au electrode were produced as mentioned above.

2.3 Materials characterization

Film morphology and thickness were characterized using scanning electron microscopy (SEM) (FEI Nova Nano-SEM450 microscope). XRD was applied to characterize the structures of Sb_2Se_3 thin films. Measurement was carried out on Philips diffractometer (X pert pro MRD using Cu Kα radiation. The standard diffraction pattern of Sb_2Se_3 is JCPDS 00-015-0861.

2.4 TOF measurement

Measurements were carried out in an optically and electrically shielded box at room temperature. TOF measurements were performed on a Keithley 2400 as the power source and an Agilent DSOS054A high-definition oscilloscope for acquiring the transient signal. Monochromatic light excitation was provided by a pulsed laser at the wavelength of 532 nm from ITO. Pulse of 78 ps duration at a frequency of 1 KHz was applied for the excitation.

2.5 TA measurement

The 400 nm thick Sb_2Se_3 film for TA measurement was fabricated by RTE on quartz substrate. The femtosecond and nanosecond TA measurements were conducted in the broadband pump-probe TA spectrometers (Helios and Eos from Ultrafast Systems, LLC). The probe (800 – 1400 nm) and pump (500 nm) are generated through nonlinear optical processes based on a fundamental pulsed laser beam provided by a Ti:Sapphire amplifier with integrated oscillator and pump laser. The wavelength and temporal width of the fundamental pulse are 800 nm and ~130 fs, respectively.

2.6 Biased IQE measurement

Before IQE measurement, we carried out transmissivity and reflectivity spectrum using Lambda 950 (Perkin Elmer). For external quantum efficiency (EQE) measurement, light source was generated by a 300 W xenon lamp of Newport (Oriel, 69911) and then split into monochromatic light using Newport oriel cornerstone^{TM} 130 1/8 Monochromator (Oriel, model 74004). A reference standard silicon solar cell was used for calibration. A Keithley 2400 source meter was used to apply bias.

2.7 Temperature dependent conductivity

I-V measurements in the temperature ranging from 85 to 420 K were performed on an Agilent B1500A in dark condition. A liquid nitrogen cryostat (Variable Temperature Insert Cryostat, CRYO Industries of America Inc.) was used to regulate the temperature.

2.8 PDS measurement

The PDS measurements were made in transverse mode [19], using reflective optics to guide the pump beam from a single grating monochromator to a sample. The pump beam was chopped at 6 Hz and was focused to a spot size of approximately 1 mm^2. The samples were kept in a helium purged glove box, until time of measurement, when they were loaded into a quartz cuvette and immersed in anhydrous perfluorohexane. The probe beam consisted of ~2 mW, 633 nm laser light from an intensity stabilized helium-neon laser. Alignment of the probe beam was made using a 3 axis stage and care was taken to avoid sample illumination from the probe beam. Probe beam deflections measured by a silicon photo-diode were amplified and processed using lock-in methods.

3 Results and discussion

3.1 Dielectric constant as a function of frequency

We have to emphasize that all the experimental characterizations presented in this paper were carried out on Sb_2Se_3 films produced by RTE because RTE so far produced the

best photovoltaic device [5]. The only exception was the cylindrical Sb_2Se_3 for dielectric constant measurement which was fabricated by hot-pressed process. Please take caution when applying the results obtained here to Sb_2Se_3 film produced by other methods since film morphology, orientation and defects could vary which would significantly influence film mobility, carrier lifetime, defect distribution and so on.

Since dielectric constant is relevant to many physical properties, we first tested the dielectric constant in the frequency range of 2 kHz to 2 MHz with an Agilent E4980A using the parallel plate capacitor configuration. The device structure is $Au/Sb_2Se_3/Au$ with the hot-pressed cylindrical Sb_2Se_3 (diameter = 13 mm, thickness = 1 mm) sandwiched between two 80 nm thick Au electrodes (as the inset in Fig. 1). The dielectric constant related to the capacitance via:

$$C = \frac{\varepsilon_r \varepsilon_0 A}{d}, \quad (1)$$

where ε_r is the dielectric constant, ε_0 is the vacuum permittivity, A is the area of electrodes, and d is the thickness of Sb_2Se_3. As shown in Fig. 1, the dielectric constant is larger than 29 at low frequency (~2 kHz) and stays approximately constant at 18 at radio-wave frequencies (~2 MHz), which is close to its optical dielectric constant of 14.3 [3]. This value is higher than copper indium diselenide (CIS, 15.2) and CdTe (10.0) in which the exciton binding energy was estimated to be 4.5 and 10.5 meV, respectively [20]. We thus believe that excitons immediately dissociate into free electrons and holes upon photon excitation in Sb_2Se_3 films, unlike in polymer absorbers where the low dielectric constant leads to strong exciton binding, which consequently necessitates a bulk heterojunction architecture for efficient exciton dissociation [21]. Free electrons and holes being the preponderant carriers in the operating device also implies their field assisted transport and compliance with the established working principles of thin film solar cells.

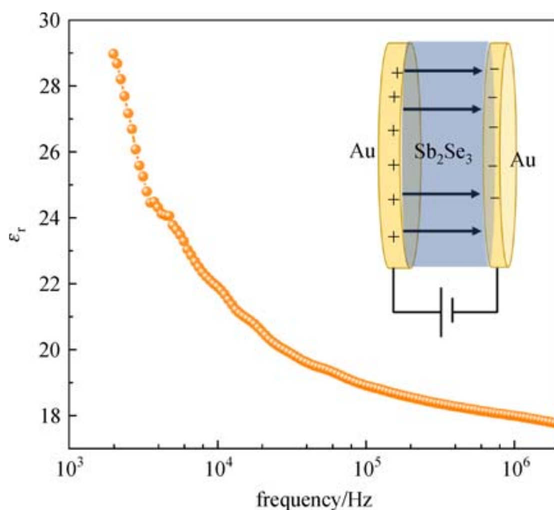

Fig. 1 Frequency dependent dielectric constant of Sb_2Se_3. The inset is the ilustration of the parallel plate capacitor with the interspcaing between Au electrodes as 1 mm

3.2 Anisotropic carrier mobility

Mobility of the absorber material is an important parameter to be considered when designing and optimizing the device configuration. Sb_2Se_3 crystal is composed of one dimensional $(Sb_4Se_6)_n$ ribbons with orthorhombic crystal structure and a space group of Pnma 62 [5]. It has strong covalent bonds along the [001] axis while only weak van der Waals bonds present in the [100] and [010] axis. For simplicity, we call direction along [100], [010] and [001] axis as *a*-, *b*- and *c*-directions, respectively. Low crystal symmetry would render high mobility anisotropy in Sb_2Se_3, which can be measured by the TOF method [22]. A valid TOF measurement need to meet the following conditions: (1) a transparent electrode allowing light illumination from at least one side, (2) pulsed excitation light with energy much larger than the material's band gap so that the absorption depth is much smaller than the sample thickness. (3) RC time constant, the product of the circuit resistance (in ohms) and the circuit capacitance (in farads), much smaller than the transit time. Our device structure for TOF measurement was $ITO/Sb_2Se_3/Au$. We used the transparent ITO glass to allow light pass through. A pulse laser with the wavelength of 532 nm corresponding to ~100 nm absorption depth in Sb_2Se_3 was used to excite a thick film Sb_2Se_3 (about 3 μm) [3]. A large number of electron-hole pairs were produced in the Sb_2Se_3 region close to ITO after the laser excitation. Electrons were quickly extracted by ITO, while holes driven by the applied bias provided by a Keithley 2400 had to travel through the thick Sb_2Se_3 films. An Agilent DSOS054A high-definition oscilloscope with max sample rate 20 GSa/s was applied to monitor the photocurrent passing through the Sb_2Se_3 layer. The hole mobility could be extracted by Eq. (2) [23]:

$$\mu_h = \frac{d^2}{V\tau_t}, \quad (2)$$

where μ_h is hole mobility, d is film thickness, V is the driving voltage varying from -0.14 to -0.08 V in a 0.02 V step and τ_t is the transit time defined by the turning point in the bilogarithmic plot of photocurrent versus decay time.

To measure the anisotropic hole mobility, [020], [120] and [221] oriented Sb_2Se_3 films on ITO substrates were produced by RTE process. [120] and [221] oriented Sb_2Se_3 films were deposited at substrate temperature of 280°C and 300°C, respectively. [020] oriented Sb_2Se_3 films were prepared at 280°C with the substrates pre-coated with 5 nm amorphous Sb_2Se_3 which was used to induce oriented growth. As shown in Fig. 2(a), the dominant X-ray diffraction peaks for the three Sb_2Se_3 films were (020),

(120) and (221). We call them as [020]-, [120]- and [221]-Sb_2Se_3 for short. Figures 2(b), 2(c) and 2(d) present the cross-sectional scanning electron microscopy images of these three films. The vertical dimension of the Sb_2Se_3 grains approximate to the thickness of Sb_2Se_3 films, suggesting carriers largely travel within a single grain during TOF measurement. As a result, the TOF derived mobility from Sb_2Se_3 films of different orientations could fully reflect the mobility anisotropy in that the possible interference caused by scattering at the grain boundaries (GBs) is minimized. Figures 2(e), 2(f) and 2(g) show the resultant normalized transient currents at various driving voltages on a bilogarithmic scale. The τ_t at various bias were determined by the intercept of the pre-transit and post-transit asymptotes of the photocurrent and marked by solid blue circles. The plots of $\tau_t \sim V^{-1}$ were plotted in the insets of Figs. 2(e), 2(f) and 2(g). Combining the slopes of $\tau_t \sim V^{-1}$ and the thickness of the [020]-, [120]- and [221]-Sb_2Se_3 films [read from Figs. 2(b), 2(c) and 2(d) as 2.8, 3.0 and 3.1 μm, respectively], the hole mobilities calculated by Eq. (2) for [020]-, [120]- and [221]-Sb_2Se_3 were 0.69, 0.81 and 1.25 $cm^2 \cdot V^{-1} \cdot s^{-1}$, respectively.

Now, we discuss the carrier transport in [020]-, [120]- and [221]-Sb_2Se_3. Figures 2(h), 2(i) and 2(j) show the (020), (120) and (221) crystal plane of Sb_2Se_3 crystal. The solid azure lines stand for the carrier transport in the $(Sb_4Se_6)_n$ ribbon connected via covalent bonds, and the red and green dash lines represent the carrier hopping from one ribbon to the adjacent ones along *a*- and *b*-directions, respectively. The shortest hopping distance along *a*- and *b*-directions are 3.29 and 3.64 Å, respectively (see Fig. S1) [24], therefore the hole mobility along the *a*-direction is expected to be larger than that along the *b*-direction. Since the mobility obtained from [020]-Sb_2Se_3 was $\mu_{h,b}$ (the hole mobility along *b*-direction, similar to $\mu_{h,a}$ and $\mu_{h,c}$), and the mobility for [120]-Sb_2Se_3 should lie between $\mu_{h,b}$ and $\mu_{h,a}$, we thus believe for hole mobility along a random direction, the following equation should hold:

$$\frac{h^2}{h^2+k^2+l^2}\mu_{h,a}^2+\frac{k^2}{h^2+k^2+l^2}\mu_{h,b}^2+\frac{l^2}{h^2+k^2+l^2}\mu_{h,c}^2=\mu_{[hkl]}^2, \tag{3}$$

where *h*, *k* and *l* are orientation index, $\mu_{[hkl]}$ is the hole mobility along [*hkl*] direction, $\mu_{h,a}$, $\mu_{h,b}$ and $\mu_{h,c}$ are the hole mobility along *a*-, *b*- and *c*-directions, respectively. The detailed derivation of Eq. (3) is shown in supplemental material [24]. Substituting [020], [120] and [221] into Eq. (3), and solving the system of linear equations, we could obtain the mobility along *a*-, *b*- and *c*-directions as 1.17, 0.69 and 2.59 $cm^2 \cdot V^{-1} \cdot s^{-2}$, respectively. $\mu_{h,c}$ is naturally the largest since this represents transport within the covalent bonded $(Sb_4Se_6)_n$ ribbon, and $\mu_{h,a}$ is larger than $\mu_{h,b}$ as the inter-ribbon distance that carriers have to hop is larger along the *b*-direction. These results reinforce our previous results that for photovoltaic applications [5], the best orientation of Sb_2Se_3 absorber is [001] oriented. In addition, we measured the conductivities of [020]-, [120]- and [221]-Sb_2Se_3 from current-voltage (*I-V*) profiles. Combining the conductivities and mobility, we calculated the free carrier density of our Sb_2Se_3 film as 1.8×10^{13} cm^{-3}, a value that is far below the optimal doping density of $\sim 10^{16}$ cm^{-3} for photovoltaic absorber layer. This is also the reason why Hall measurements carried out at room temperature on our RTE processed Sb_2Se_3 films always fail.

We succeeded in Hall measurement on our Sb_2Se_3 films at elevated temperature due to sufficient thermally excited carriers. At 380 K, Sb_2Se_3 is dominated by "intrinsic excitation" (discussed below), and the mobility obtained from Hall measurement is $|\mu_e - \mu_h|$ (Please refer to supplemental material for detailed discussion [24]), where μ_e and μ_h are electron and hole mobility, respectively. By repeating the Hall measurement at 380 K 10 times, the resultant average $|\mu_e - \mu_h|$ values for [020]-, [120]- and [221]-Sb_2Se_3 were (24.1±2.3), (12.1±2.1), and (8.9±1.9) $cm^2 \cdot V^{-1} \cdot s^{-1}$, respectively. Assuming the mobility is mainly affected by acoustic scattering, the mobility is proportional to $T^{-3/2}$. The Hall mobilities at room temperature (298 K) for [020]-, [120]- and [221]-Sb_2Se_3 were thus estimated as (16.9±1.6), (8.5±1.5), and (6.2±1.3) $cm^2 \cdot V^{-1} \cdot s^{-1}$, respectively. Please note that for the Van der Pauw method of Hall measurement, the measured mobility is along the horizontal direction and is thus loosely relevant to the orientation of the Sb_2Se_3 film. Consequently, we cannot derive the electron mobility along the *a*-, *b*- and *c*-directions using Eq. (3). We know, for sure, that the electron mobility along *c*-direction is larger than 16.9 $cm^2 \cdot V^{-1} \cdot s^{-1}$ at room temperature because the measured Hall mobility was reduced by the scattering of grain boundaries when electrons travel through multiple grain boundaries in current Hall measurement. Moreover, the measured negative hall coefficient indicates that the electron mobility is larger than hole mobility which is consistent with our experiment result.

3.3 Carrier dynamics and lifetime

We applied time-resolved femtosecond (fs-TA) and nanosecond (ns-TA) transient absorption spectrum to study the dynamics of photogenerated carriers in [221]-Sb_2Se_3 thin films on quartz substrate with the thickness of 400 nm. The fs-TA and ns-TA measurements were conducted in the broadband pump-probe TA spectrometers (Helios and Eos from Ultrafast Systems, LLC). The probe (800 – 1400 nm) and pump (500 nm) are generated through nonlinear optical processes based on a fundamental pulsed

laser beam provided by a Ti:Sapphire amplifier with integrated oscillator and pump laser. The wavelength and temporal width of the fundamental pulse are 800 nm and ~130 fs, respectively [25]. Because the pump photon energy is significantly higher than bandgap (1.17 eV) [3], the charge carriers initially created should be hot carriers. Figure 3(a) shows TA spectral evolution with respect to delay time. At short delay (0.3 ps, blue trace), a sharp photo-induced absorption (PIA) band peaks at 900 nm, which quickly evolves to dispersive line shape (3 ps, green trace). The PIA is attributed to the hot carrier induced band gap renormalization [26], and then the fast spectral evolution implies the short intraband relaxation. The dispersive TA spectrum is also observed in other indirect bandgap semiconductors (e.g. multi-layer MoS_2), in which the photon-induced bleach and absorption were attributed to band-filling and transition broadening, respectively, by thermalized carriers at direct (or indirect) conduction band edge [27]. As the delay increases, the dispersive line shape evolves to a broad PIA band extends from 800 nm to > 1300 nm (300 ps, red traces), and this process is relatively slow, on the time scale of ~100 ps. Because our Sb_2Se_3 has a small difference in energy between indirect (1.04 eV) and direct (1.17 eV) band gaps, the broad PIA band is attributed to the carrier re-distribution within the indirect and direct band gaps. Within 5 ns, the broad PIA band stops evolving, suggesting the long lifetime of the carriers at indirect band gap states. The three-phase dynamics is more clearly shown by the TA kinetics averaged between 900 and 950 nm (Fig. 3(b)), phase I, II, and III). To monitor the depopulation of the trapped carriers due to charge recombination, the kinetics of the broad PIA band is also measured by using ns-TA setup, which is shown in Fig. 3(c). The carrier lifetime is determined to be (67±7) ns by the exponential fit.

3.4 Minority carrier diffusion length

Our RTE derived Sb_2Se_3 thin film is weakly p-type, and the minority carrier (electron) diffusion length along *c*-

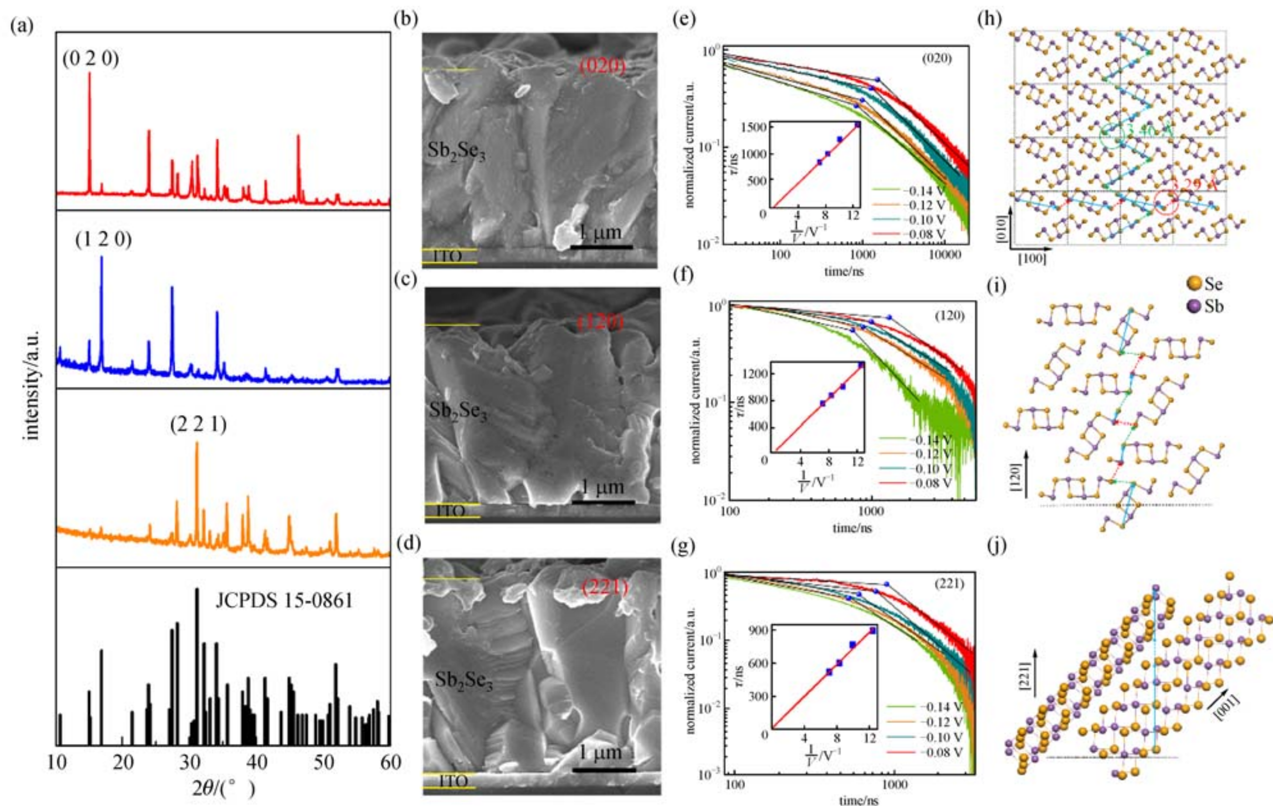

Fig. 2 Estimation of anisotropic carrier mobilities. (a) X-ray diffraction patterns of [020]-, [120]- and [221]-Sb_2Se_3 films and (b–d) the corresponding cross-sectional SEM image. The transient current in TOF measurement of (e) [020]-Sb_2Se_3, (f) [120]-Sb_2Se_3 and (g) [221]-Sb_2Se_3 films after photoexcitation at time $t = 0$ in a bilogarithmic plot; the transit time τ_t is identified as the crossover point of two blue lines. The atomic configuration of (h) (020), (i) (120) and (j) (221) crystal plane of Sb_2Se_3. The red and green dash arrows represent the carrier hopping from one ribbon to the adjacent ones along *a*- and *b*-directions, respectively; the azure solid arrows stand for carrier transporting within the $(Sb_4Se_6)_n$ ribbons

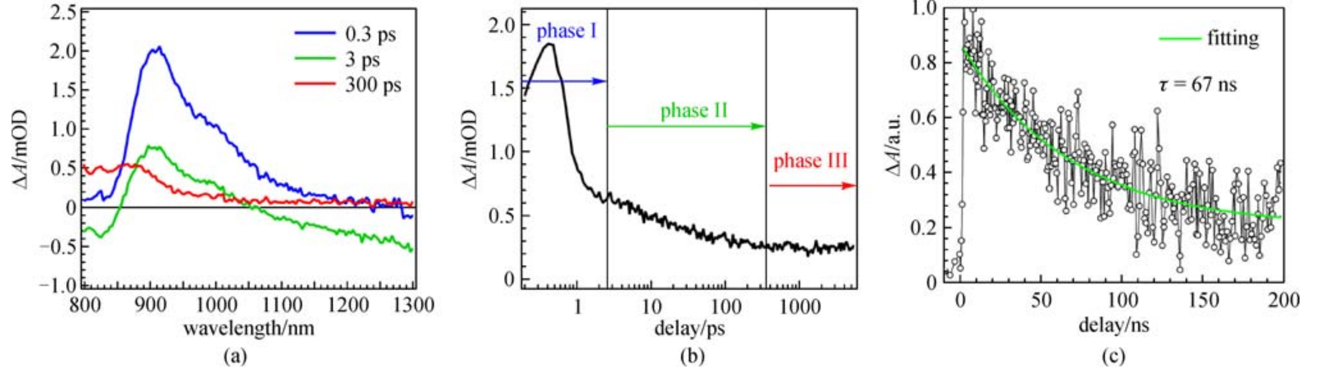

Fig. 3 (a) TA spectrum at various time delays after photoexcitation; (b) fs-TA kinetics averaged between 900 and 950 nm; (c) ns-TA edge kinetics averaged between 900 and 950 nm and the corresponding single exponential fitting (green lines) for Sb_2Se_3 film

direction, $L_{e,c}$ is a parameter that heavily influences photovoltaic performance. $L_{e,c}$ can be estimated by Eq. (4):

$$L_{e,c} = \sqrt{D_{e,c}\tau_e} = \sqrt{\frac{\mu_{e,c}\tau_e k_B T}{q}}, \tag{4}$$

where $D_{e,c}$ is the electron diffusion coefficient along c-direction, $\mu_{e,c}$ is electron mobility along c-direction, k_B is the Boltzmann constant, T is the absolute temperature, q is the elementary charge, and τ_e is the electron lifetime. From the mobility (16.9 $cm^2 \cdot V^{-1} \cdot s^{-1}$) and lifetime (67 ns) parameters, we obtain the electron diffusion length of (1.7±0.2) μm along c-direction. Since both the electron lifetime and mobility are strongly carrier-density dependent, and both the TA and TOF measurement were carried out under high illumination, we believe as-calculated diffusion length is valid only under strong irradiation. We thus further applied the bias voltage dependent IQE to deduce the diffusion length under weak light illumination (xenon lamp spectrum of ~150 $\mu W \cdot cm^{-2}$ during IQE measurement) [28]. The device structure for extracting diffusion length is ITO/CdS/Sb_2Se_3/Au (inset in Fig. 4(a)) with PCE of 5.4% (Voc = 0.391 V, Jsc = 25.2 $mA \cdot cm^{-2}$ and FF = 54.7%). The orientation of thin film Sb_2Se_3 was [221]. Extraction from this technique was done using the following steps in sequence: (1) measuring EQE(λ, V) as a function of wavelength (λ) at a series of voltage bias (V); (2) determining the reflectivity $R(\lambda)$ and transmittance $T(\lambda)$ as a function of wavelength; (3) calculating internal quantum efficiency, IQE(λ, V) using the relation of IQE(λ, V) = EQE(λ, V)/[$1 - R(\lambda) - T(\lambda)$] (the test method was as shown in supplemental material [24]); (4) obtaining the voltage dependence of depletion width $x_d(V)$ from capacitance-voltage (C-V) measurement; (5) obtaining the dependence of x_d on IQE at each λ; (6) extracting diffusion length (L_e) and absorption coefficient (α) from the expression given by Eq. (5) [29].

$$-\ln(1 - \mathrm{IQE}) = \alpha x_d + \ln(1 + \alpha L_e). \tag{5}$$

Equation (5) is valid only when all carriers generated within the depletion region are completely collected while the carriers generated in the quasi-neutral region are collected with an exponentially decaying probability with the length scale, defined by the minority carrier diffusion length. In our device, the thickness of Sb_2Se_3 was 743 nm, and the depletion width was approximately 335 nm obtained from C-V measurement, which meant that the quasi-neutral region was about 408 nm where photogenerated carriers are collected by diffusion. The bias dependence of IQE and C-V was show in Figs. S2 and S3 [24]. The measured values of $-\ln(1-\mathrm{IQE})$ as function of x_d for various wavelengths are shown in Fig. 4(a). The diffusion length of minority carrier as (0.29±0.03) μm which was measured under xenon lamp illumination with an intensity of 150 $\mu W \cdot cm^{-2}$ was extracted by the intercept from Eq. (5). And the direction of diffusion length was corresponding to the orientation of [221]-Sb_2Se_3. To test our assumptions and thus lend credibility to our result, we verified consistency between the absorption coefficient obtaining from the slope of Eq. (5) (red dots line in Fig. 4 (b)) and the measured value derived from transmittance (black line in Fig. 4(b)). We thus conclude that depending on the illumination intensity, the carrier diffusion length within our RTE produced Sb_2Se_3 film is between 0.29 and 1.7 μm.

3.5 Defect depth

Temperature dependent dark conductivity was measured to investigate defect types and depths in our Sb_2Se_3 thin films with [221] orientation. We used a symmetric device structure, Au/Sb_2Se_3/Au, with glass as the substrates and Au electrodes with a spacing of 200 μm as the Ohmic contacts. I-V measurements in the temperature ranging from 85 to 420 K were performed on an Agilent B1500A in dark condition. A liquid nitrogen cryostat (Variable Temperature Insert Cryostat, CRYO Industries of America Inc.) was used to regulate the temperature. Resistances were evaluated around the zero-bias voltage from I-V data by linear least-square fitting.

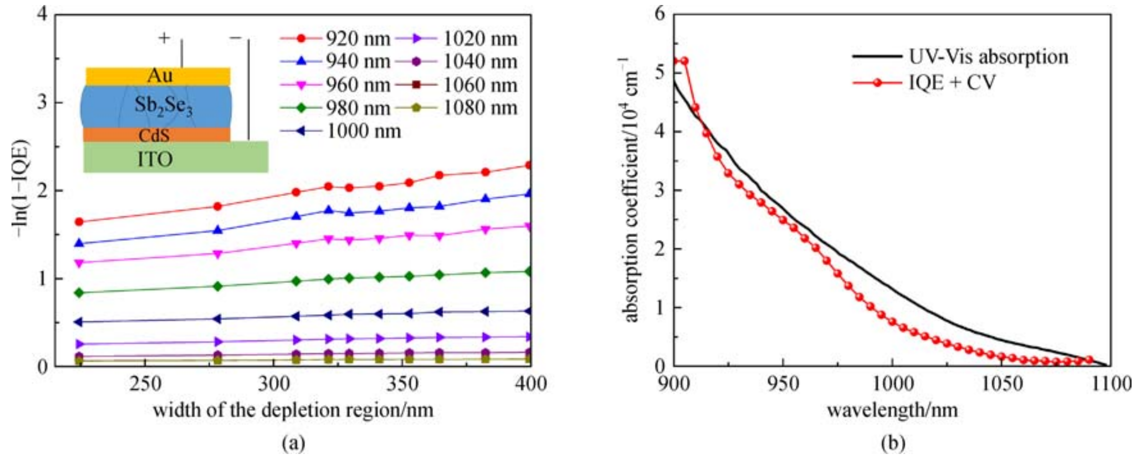

Fig. 4 Estimation of diffusion length by the bias dependent IQE method. (a) –ln(1 –IQE) against depletion width (x_d). The diffusion length and absorption coefficient were extracted by the intercept and slope of the linear fitting. (b) Comparison between the absorption coefficient derived from IQE + CV (red dots line) and the measured value from transmittance (black line)

The conductivity of Sb_2Se_3 film at 85 to 420 K was in the order of 10^{-4} to 10^{-11} S·cm^{-1} (see Fig. 5(a)). We identify two different transport mechanisms. At high temperatures (above 160 K), the electrical conductivity depends on the number of carriers thermally activated from the defects to the band, which again depend on defect depth and temperature, as shown in Eq. (6) [30]:

$$\sigma = \sigma_1 \exp\left(-\frac{E_1}{k_B T}\right) + \sigma_2 \exp\left(-\frac{E_2}{k_B T}\right), \quad (6)$$

where $E_{1,2}$ is the activation energies and $\sigma_{1,2}$ is the pre-exponential factor, k_B is Boltzmann constant and T is the absolute temperature. Two linear regions were observed in Fig. 5(a) (lnσ against 1000/T), and the corresponding activation energies were obtained by fitting Eq. (6). Between 250 and 420 K, the activation energy E_1 is (0.578±0.009) eV, which is approximately half of the direct band gap (1.17 eV) of Sb_2Se_3. In this temperature region, intrinsic excitation dominates the carrier density. Between 160 and 250 K, the fitted activation energy E_2 was (0.111±0.005) eV, corresponding to a defect depth of 0.111 eV. This defect is ascribed to the acceptor defect of Se_{Sb} as suggested by theoretical calculation that Se_{Sb} has the lowest formation energy and is a shallow acceptor with defect depth of approximately 0.1 eV [31]. In the low temperature region (85 – 160 K), the conductivity is slowly reduced with the temperature because the conduction mechanism change into Mott's variable range hopping between localized states [32]. The conductivity as a function of temperature is described in Eq. (7):

$$\sigma(T) = \sigma_0' T^{-1/2} \exp[-(T_0/T)^{1/4}], \quad (7)$$

where T_0 is a characteristic temperature which is related to the disorder of the material, σ_0' is a constant, and T is

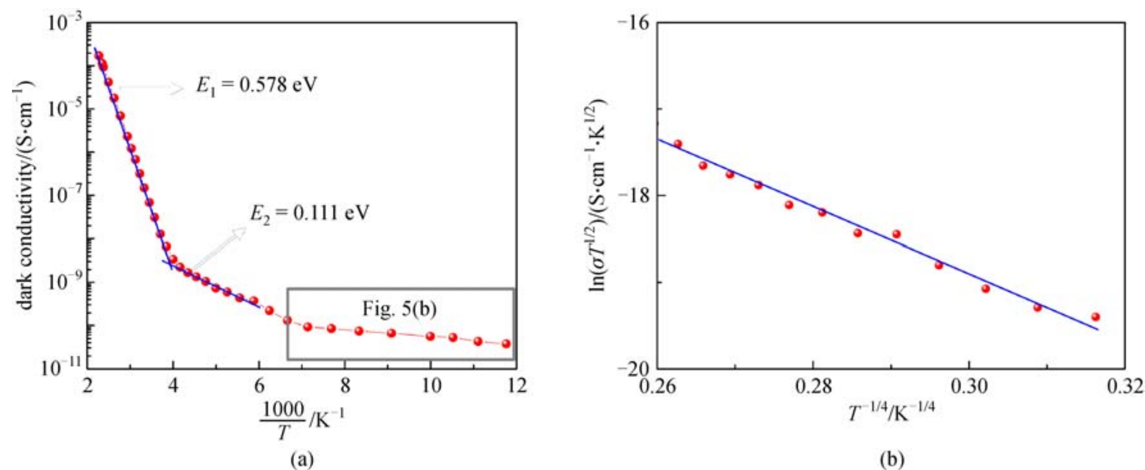

Fig. 5 Defect characterization on [221] oriented Sb_2Se_3 by temperature dependent conductivity measurement. (a) Logarithmic dark conductivity versus 1000/T in the temperature range of 85 to 420 K; (b) ln($\sigma T^{1/2}$) versus $T^{-1/4}$ in the temperature range of 85 to 160 K

the absolute temperature. Figure 5(b) shows the plot of $\ln(\sigma T^{1/2})$ against $T^{-1/4}$. It is clear that the relation is linear, which indicates the occurrence of a hopping conduction mechanism and from which we can calculate the characteristic temperature T_0 as 2.31×10^6 K. This value is larger than the values of CZTS and CIGS [33], implying more disorder in our Sb_2Se_3 films.

3.6 Density of defect states

As discussed above, we believe shallow acceptor Se_{Sb} was the dominant defects in our Sb_2Se_3 films produced by RTE. Using the T. Walter's method [34], we could extract the density of defect states from thermal admittance spectroscopy (TAS). Device configuration for TAS measurement was ITO/CdS/Sb_2Se_3/Au as the inset in Fig. 4(a), our standard superstrate solar cell configuration. The experiments were performed using Keithley 4200-CVU module with frequencies ranging from 1 kHz to 10 MHz. The energy profile of trap density of states (N_t) can be derived from the angular frequency dependent capacitance according to Eq. (8) [34]:

$$N_t(E_\omega) = -\frac{V_{bi}}{qx_d}\frac{dC}{d\omega}\frac{\omega}{k_B T}, \tag{8}$$

where C is the capacitance, ω is the angular frequency ($\omega = 2\pi f$), q is the elementary charge, k_B is the Boltzmann constant and T is absolute temperature. V_{bi} and x_d are the built-in potential and depletion width, respectively, which were extracted from C-V measurement. The applied angular frequency ω defines an energetic demarcation as Eq. (9) [34]:

$$E_\omega = k_B T \ln\left(\frac{\omega_0}{\omega}\right), \tag{9}$$

where E_ω is the energy depth of the defect relative to the corresponding band edge, ω_0 is the attempt-to-escape frequency which is related to defect capture cross section, effective density of states in the valence band, and thermal velocity. Figure 6(a) is the density of defect states. There was a Gaussian defect peak in the gap with the peak position at (0.095±0.008) eV, which was consistent with the defect depth of (0.111±0.005) eV obtained from temperature dependent conductivity measurement. The profile of the defect distribution is shown in Fig. 6(b). The density of defect states was about 10^{16} $cm^{-3}\cdot eV^{-1}$ at the peak position and the integrated defect density was 1.3×10^{15} cm^{-3}.

The defect density could also be extracted from space charge limited current (SCLC) measurement [35] at the transition regime between the linear region and the quadratic region (as seen in supplemental material [24]). The trap density n_t was 6.9×10^{14} cm^{-3} based on the SCLC result, in good agreement with the value obtained from TAS. We should emphasize that our first-principle calculation using VSAP code also predicted an equilibrium defect density of 1×10^{15} cm^{-3} for Sb_2Se_3 film at room temperature [31], thus validating our experimental results. Assuming the probability of defect activation dictated by the Fermi-Dirac distribution as $1/\{1 + \exp[(E_t - E_F)/kT]\}$, the activated percentage of defects would be 3.4% corresponding to the extremely low doping density of 2.4×10^{13} cm^{-3}, echoing our previous carrier density measurement.

3.7 Optical band tail

Band tails in the optical absorption band edges are observed in many disorder materials. For photovoltaic applications, the local band tail state can lead to the degradation of device performance particularly for V_{OC}. It can be caused by doping or disorder due to the destruction

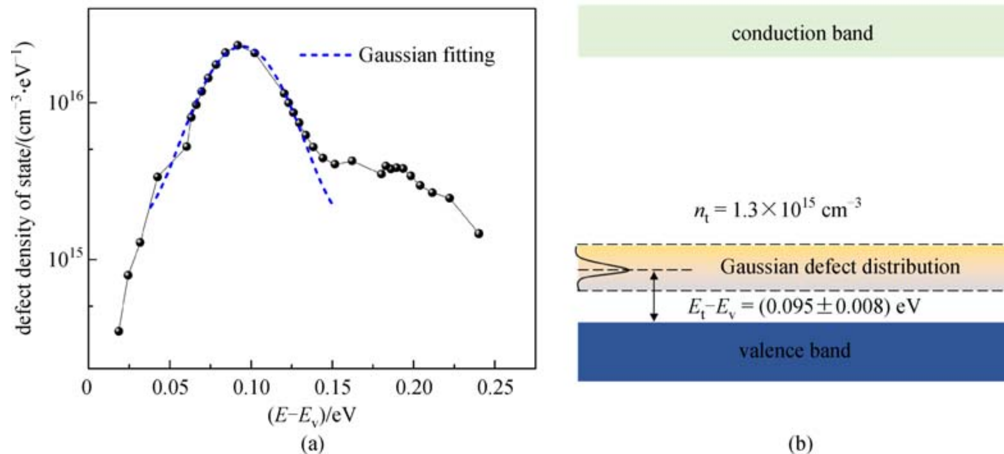

Fig. 6 Defect distribution in Sb_2Se_3 film. (a) Density of defect states of Sb_2Se_3 from admittance spectra. The defect peak at (0.095±0.008) eV could be perfectly fitted by Gaussian function as blue dash line; (b) Gaussian defect distribution in the band gap

of the lattice periodicity. The band tail can be investigated by photothermal deflection spectroscopy (PDS), which is widely used to examine the optical properties of materials [19]. The devices for PDS measurement were prepared by depositing 1000 nm crystalline (c-Sb_2Se_3) films on quartz glass using RTE. PDS spectra were acquired from 0.6 to 2.5 eV, and were subsequently repeated over the course of several days. We found no appreciable change in the PDS signal, thus verifying the stability of these materials against the index fluid, perfluorohexane. The detailed test process is shown in supplemental material [24]. We obtained absorption coefficients by first system correcting the raw data using a "blackbody" spectrum from a graphite thin film painted on glass substrates identical to those used for sample growth. We then scaled the PDS spectra to make the above gap data consistent with absorptance, $A = 1-R-T$ (R and T represent reflectance and transmittance, respectively), data that was obtained with a Cary 2500 and integrating sphere. Lastly we converted the absorptance to absorption coefficient (α) using Eq. (10), neglecting reflections from the film-substrate interface [36],

$$\alpha = \frac{1}{d}\ln\left(1 + \frac{A}{T}\right), \tag{10}$$

where d is the sample thickness. The PDS spectrum were shown in Fig. 7. The Urbach energy was estimated from fitting the exponential band-edge portion of the absorption coefficient versus energy plot by Eq. (11) [37].

$$\alpha = \alpha_0 \exp[(h\nu - U_1)/U_0], \tag{11}$$

where $h\nu$ is the photon energy, U_0 is the Urbach energy, U_1, and α_0 are constants determined by fits to experiment. In the energy range of 1.1 to 1.25 eV, the Urbach energy is (38±3) meV. Another extremely large Urbach energy ((129±7) meV) was observed in lower energy region (0.8 to 1.1 eV) in the crystal Sb_2Se_3 spectra. This unusually large value may result not from the Sb_2Se_3 film, but from other non-stoichiometric phases in the film that occur during growth in non-optimal conditions. For example, the presence of oxygen during growth may consume antimony and leave selenium rich regions, which are more disordered. These observations (i.e. antimony oxides, etc.) help explain the low device performance for our Sb_2Se_3 solar cells, and motivate further optimization of growth conditions.

To test this speculation, we measured the PDS spectra of amorphous Sb_2Se_3 film (black dots in Fig. 7) which was completely disordered and then compared it to the crystalline counterparts (red dots in Fig. 7). A-Sb_2Se_3 film was deposited by thermal evaporation (TE) with the substrate kept at room temperature. The a-Sb_2Se_3 PDS spectra showed only one exponential region with Urbach energy (79±2) meV, while in the crystalline samples, the large Urbach energy region begins near 1 eV.

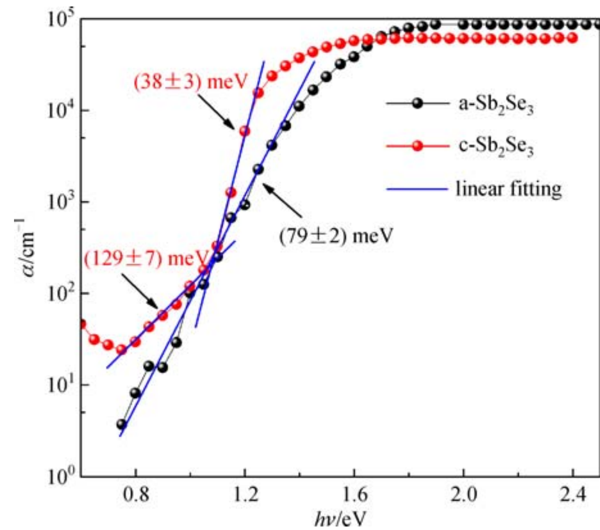

Fig. 7 Absorption coefficient (α) versus photon energy ($h\nu$). The Absorption coefficient of crystal and amorphous Sb_2Se_3 films were obtain from PDS spectrum

4 Discussion

The obtained physical properties of RTE deprived Sb_2Se_3 film are summarized in Table 1. We now discuss the cons and pros of our Sb_2Se_3 thin films in terms of optoelectronic properties, as well as the suggested strategies for further efficiency improvement based on our characterization.

First, we argue that pseudo-direct optical transition nature of Sb_2Se_3 might be beneficial for photovoltaic application. For our Sb_2Se_3, the lowest indirect band gap (E_{ind}) is 1.04 eV and the lowest direct band gap (E_d) is 1.17 eV at room temperature [3], which means Sb_2Se_3 absorption starts at 1192 nm and then changes to strong absorption at 1060 nm due to the p- > p transition [38] and direct band gap. Presently, absorption is not a limiting factor, as J_{SC} of 25 mA·cm^{-2} was obtained in our certified device with the Sb_2Se_3 absorber of only 390 nm thickness. One natural advantage of pseudo-direct band gap is the long carrier lifetime owning to the phonon-assisted recombination nature. The TA derived carrier lifetime is 67 ns, which is shorter than $CH_3NH_3PbI_3$ (288 ns from TA measurement) [39] and the best CdTe single crystals (400 ns, single-photon counted decay) [40], but significantly longer than CZTSSe (6.7 ns measured from photoluminescence decay) [41], CIGS (5.5 ns measured from photoluminescence decay) [42] and SnS (< 100 ps measured from transient terahertz photoconductivity) [43]. One further advantage associated with high absorption coefficient and long carrier lifetime is that Sb_2Se_3 can maintain high non-equilibrium carrier density under AM1.5G illumination, thus permitting large Fermi level splitting and higher open circuit voltages.

Second, we discuss the implication of the measured mobility of our Sb_2Se_3 film. The along-ribbon mobility of

Table 1 Summary of physical parameters of Sb_2Se_3 reported in this paper

parameter		value	characterization method
ε_r		18	CF, 2 MHz
		29	CF, 2 kHz
$\mu_h/(cm^2 \cdot V^{-1} \cdot s^{-1})$	*a*	1.17	TOF
	b	0.69	
	c	2.59	
$\mu_e/(cm^2 \cdot V^{-1} \cdot s^{-1})$	*c*	> 16.9	Hall effect
τ_e/ns		67±7	TA
L_e/μm	[221]	0.29±0.03	bias IQE, low illumination
	[001]	1.7±0.2	calculated, high illumination
n_t/cm^{-3}		6.9×10^{14}	SCLC
		1.3×10^{15}	TAS
$(E_t - E_v)$/eV		0.095±0.008	TAS
E_1/eV		0.578±0.009	conductivity
E_2/eV		0.111±0.005	conductivity
T_0/K		2.31×10^6	conductivity
U_0/meV	c-Sb_2Se_3	38±3	(1.1 – 1.25 eV) PDS
	c-Sb_2Se_3	129±7	(0.8 – 1.1 eV) PDS
	a-Sb_2Se_3	79±2	(0.8 – 1.25 eV) PDS

Sb_2Se_3 lies in 1 – 20 $cm^2 \cdot V^{-1} \cdot s^{-1}$, better than PbS CQDs (0.001 – 0.1 $cm^2 \cdot V^{-1} \cdot s^{-1}$) [44], Cs_2SnI_6 (2.9 $cm^2 \cdot V^{-1} \cdot s^{-1}$) [45] and $CuZnSn(S,Se)_4$ (0.5 – 1.3 $cm^2 \cdot V^{-1} \cdot s^{-1}$) [46] yet worse than Bi_2S_3 (257 $cm^2 \cdot V^{-1} \cdot s^{-1}$) [47], $CH_3NH_3PbI_3$ (15 – 40 $cm^2 \cdot V^{-1} \cdot s^{-1}$) [48] and SnS (128 $cm^2 \cdot V^{-1} \cdot s^{-1}$) [49]. Mediocre carrier mobility in combination with the better-than-average carrier lifetime results in a decent diffusion length approaching 1.7 μm under strong light illumination, which is much better than PbS CQDs solid which has strived for > 300 nm diffusion length for years and now has obtained certified device efficiency of 10.7% [50]. The concern is the highly anisotropic nature of mobility due to its one-dimensional crystal structure. Stringent control of *c*-axis oriented film is imperial for high efficiency thin film solar cells, and preliminary success was obtained through deposition temperature control.

Last we would discuss the defects and doping density in Sb_2Se_3. Previous theoretical simulation, and the present experimental results included here suggest that the dominant defect in Sb_2Se_3 film produced by RTE strategy is Se_{Sb} acceptor with defect depth of ~0.1 eV and density of ~1×10^{15} cm^{-3}. Defect depth is acceptable yet shallower defects such as V_{Cu} in CIGS with a depth of ~0.03 eV is preferable. The doping density (~10^{13} cm^{-3}) is far lower than the optimal value of approximately 10^{16} cm^{-3} for the absorber layer in a photovoltaic device. Whether this is intrinsic for this material, or it is because of the strong compensation by defect pairs remains elusive at this stage. Strategies to significantly increase carrier density in Sb_2Se_3 film deserve further efforts. Alternatively, construction of device with p-i-n configuration, in analogy to heterostructure with intrinsic thin layer (HIT) silicon or perovskite solar cell, would probably circumvent this obstacle. In addition, the large band tail in our Sb_2Se_3 films is harmful to solar cells. However, it may be overcome by supplementing Se element, increasing the crystallinity and eliminating the secondary phase such as Sb_2O_3.

5 Conclusion

In conclusion, we have systematically studied the photovoltaic relevant physical properties of Sb_2Se_3 film produced from RTE. The dielectric constant of Sb_2Se_3 is measured to be between 29 to 18 within the frequency 2 kHz – 2 MHz. TOF measurements revealed that the hole mobility in a single Sb_2Se_3 grain along *a*-, *b*- and *c*-directions were 1.17, 0.69 and 2.59 $cm^2 \cdot V^{-1} \cdot s^{-2}$, respectively. Hall measurement at elevated temperature suggested that the electron mobility along *c*-direction was larger than 16.9 $cm^2 \cdot V^{-1} \cdot s^{-1}$. Fs-TA and ns-TA spectrum illustrated the non-equilibrium carrier dynamics upon photoexcitation, and the minority carrier lifetime was fitted as (67±7) ns based on TA characterization. The electron diffusion length along *c*-direction under high illumination was (1.7±0.2) μm, while under low illumination along the [221] direction was (0.29±0.03) μm. Temperature dependent dark conductivity measurement

indicated two thermal activation energies of (0.578±0.009) eV and (0.111±0.005) eV, corresponding to intrinsic thermal excitation and defect activation, respectively. Admittance spectroscopy was used to determine the density of defect states in the order of 10^{16} $cm^{-3}\cdot eV^{-1}$ and the position of defect peaked at (0.095±0.008) eV. The corresponding integrated defect density is 1.3×10^{15} cm^{-3} which is in good agreement with that of 6.9×10^{14} cm^{-3} obtained from SCLC. The free carrier density was about 1.8×10^{13} cm^{-3}. The Urbach energy of c-Sb_2Se_3 is (38±3) meV in the range of 1.1 to 1.25 eV and (129±7) meV in the range of 0.8 to 1.1 eV, while the Urbach energy of a-Sb_2Se_3 is (79±2) meV in the range of 0.8 to 1.25 eV. The reasonably good optoelectronic properties revealed here, coupled with its excellent material properties such as simple and stable phase, non-toxic and low-cost constituents, rendering our Sb_2Se_3 stands out among many emerging absorber materials and thus deserving further extensive study.

Acknowledgements This work was supported by the National Key Research and Development Program of China (No. 2016YFA0204000), the National Natural Science Foundation of China (NSFC) (Grant Nos. 61322401 and 91433105), the Special Fund for Strategic New Development of Shenzhen, China (No. JCYJ20160414102210144) and "National 1000 Young Talents" project. Professor Shiyou Chen at East China Normal University is acknowledged for helpful discussions. The authors would like to thank the Analytical and Testing Center of HUST and the Center for Nanoscale Characterization and Devices of WNLO for the characterization support.

References

1. Petzelt J, Grigas J. Far infrared dielectric dispersion in Sb_2S_3, Bi_2S_3 and Sb_2Se_3 single crystals. Ferroelectrics, 1973, 5(1): 59–68
2. Zhou Y, Leng M, Xia Z, Zhong J, Song H, Liu X, Yang B, Zhang J, Chen J, Zhou K, Han J, Cheng Y, Tang J. Solution-processed antimony selenide heterojunction solar cells. Advanced Energy Materials, 2014, 4(8): 1301846
3. Chen C, Li W, Zhou Y, Chen C, Luo M, Liu X, Zeng K, Yang B, Zhang C, Han J, Tang J. Optical properties of amorphous and polycrystalline Sb_2Se_3 thin films prepared by thermal evaporation. Applied Physics Letters, 2015, 107(4): 043905
4. Ghosh G. The Sb-Se (antimony-selenium) system. Journal of Phase Equilibria, 1993, 14(6): 753–763
5. Zhou Y, Wang L, Chen S, Qin S, Liu X, Chen J, Xue D J, Luo M, Cao Y, Cheng Y, Sargent E H, Tang J. Thin-film Sb_2Se_3 photovoltaics with oriented one-dimensional ribbons and benign grain boundaries. Nature Photonics, 2015, 9(6): 409–415
6. Luo M, Leng M, Liu X, Chen J, Chen C, Qin S, Tang J. Thermal evaporation and characterization of superstrate CdS/Sb_2Se_3 solar cells. Applied Physics Letters, 2014, 104(17): 173904
7. Liu X, Chen J, Luo M, Leng M, Xia Z, Zhou Y, Qin S, Xue D J, Lv L, Huang H, Niu D, Tang J. Thermal evaporation and characterization of Sb_2Se_3 thin film for substrate Sb_2Se_3/CdS solar cells. ACS Applied Materials & Interfaces, 2014, 6(13): 10687–10695
8. Leng M, Luo M, Chen C, Qin S, Chen J, Zhong J, Tang J. Selenization of Sb_2Se_3 absorber layer: an efficient step to improve device performance of CdS/Sb_2Se_3 solar cells. Applied Physics Letters, 2014, 105(8): 083905
9. Liu X, Chen C, Wang L, Zhong J, Luo M, Chen J, Xue D J, Li D, Zhou Y, Tang J. Improving the performance of Sb_2Se_3 thin film solar cells over 4% by controlled addition of oxygen during film deposition. Progress in Photovoltaics: Research and Applications, 2015, 23(12): 1828–1836
10. Sinsermsuksakul P, Sun L, Lee S W, Park H H, Kim S B, Yang C, Gordon R G. Overcoming efficiency limitations of SnS-based solar cells. Advanced Energy Materials, 2014, 4(15): 1400496
11. Solar Frontier Achieves World Record Thin-Film Solar Cell Efficiency: 22.3%, http://www.solar-frontier.com/eng/news/2015/C051171.html (accessed: November, 2016)
12. First Solar pushes CdTe cell efficiency to record 22.1%, http://www.pv-tech.org/news/first-solar-pushes-cdte-cell-efficiency-to-record-22.1 (accessed: November, 2016)
13. Wang W, Winkler M T, Gunawan O, Gokmen T, Todorov T K, Zhu Y, Mitzi D B. Device characteristics of CZTSSe thin-film solar cells with 12.6% efficiency. Advanced Energy Materials, 2014, 4(7): 1301465
14. Sai H, Matsui T, Koida T, Matsubara K, Kondo M, Sugiyama S, Katayama H, Takeuchi Y, Yoshida I. Triple-junction thin-film silicon solar cell fabricated on periodically textured substrate with a stabilized efficiency of 13.6%. Applied Physics Letters, 2015, 106(21): 213902
15. Black J, Conwell E M, Seigle L, Spencer C W. Electrical and optical properties of some $M_2^{V\text{-}B}N_3^{VI\text{-}B}$ semiconductors. Journal of Physics and Chemistry of Solids, 1957, 2(3): 240–251
16. Benjamin S L, de Groot C H, Hector A L, Huang R, Koukharenko E, Levason W, Reid G. Chemical vapour deposition of antimony chalcogenides with positional and orientational control: precursor design and substrate selectivity. Journal of Materials Chemistry C, Materials for Optical and Electronic Devices, 2015, 3(2): 423–430
17. Gilbert L R, Van Pelt B, Wood C. The thermal activation energy of crystalline Sb_2Se_3. Journal of Physics and Chemistry of Solids, 1974, 35(12): 1629–1632
18. Ma J, Su T, Li M D, Du W, Huang J, Guan X, Phillips D L. How and when does an unusual and efficient photoredox reaction of 2-(1-hydroxyethyl) 9,10-anthraquinone occur? A combined time-resolved spectroscopic and DFT study. Journal of the American Chemical Society, 2012, 134(36): 14858–14868
19. Jackson W B, Amer N M, Boccara A C, Fournier D. Photothermal deflection spectroscopy and detection. Applied Optics, 1981, 20(8): 1333–1344
20. Madelung O. Semiconductors: Data Handbook. New York: Springer Science & Business Media, 2012
21. Engel M, Kunze F, Lupascu D C, Benson N, Schmechel R. Reduced exciton binding energy in organic semiconductors: tailoring the Coulomb interaction. Physica Status Solidi (RRL)-Rapid Research Letters, 2012, 6(2): 68–70
22. Pavlica E, Bratina G. Time-of-flight mobility of charge carriers in position-dependent electric field between coplanar electrodes.

Applied Physics Letters, 2012, 101(9): 093304
23. Haynes J R, Shockley W. The mobility and life of injected holes and electrons in Germanium. Physical Review, 1951, 81(5): 835–843
24. Supplemental Material at http://link.springer.com/article/10.1007/s12200-017-0702-z for the detailed derivation of Eq. (3) and Hall mobility formula, biased IQE, PDS and SCLC, CV measurements, and the inter-atom distances in Sb_2Se_3
25. Yang Y, Rodríguez-Córdoba W, Lian T. Ultrafast charge separation and recombination dynamics in lead sulfide quantum dot-methylene blue complexes probed by electron and hole intraband transitions. Journal of the American Chemical Society, 2011, 133(24): 9246–9249
26. Yang Y, Ostrowski D P, France R M, Zhu K, van de Lagemaat J, Luther J M, Beard M C. Observation of a hot-phonon bottleneck in lead-iodide perovskites. Nature Photonics, 2016, 10(1): 53–59
27. Shi H, Yan R, Bertolazzi S, Brivio J, Gao B, Kis A, Jena D, Xing H G, Huang L. Exciton dynamics in suspended monolayer and few-layer MoS_2 2D crystals. ACS Nano, 2013, 7(2): 1072–1080
28. Gokmen T, Gunawan O, Mitzi D B. Minority carrier diffusion length extraction in $Cu_2ZnSn(Se,S)_4$ solar cells. Journal of Applied Physics, 2013, 114(11): 114511
29. Liu X X, Sites J R. Solar-cell collection efficiency and its variation with voltage. Journal of Applied Physics, 1994, 75(1): 577–581
30. Seto J Y W. The electrical properties of polycrystalline silicon films. Journal of Applied Physics, 1975, 46(12): 5247–5254
31. Liu X, Xiao X, Yang Y, Xue D J, Li D, Chen C, Lu S, Gao L, He Y, C B M, Wang G, Chen S, Tang J. Enhanced Sb_2Se_3 solar cell performance through theory-guided defect control. Submitted to Progress in Photovoltaics: Research and Applications
32. Mott N F, Davis E A. Electronic Processes in Non-Crystalline Materials. Oxford: Oxford University Press, 2012
33. Guo B L, Chen Y H, Liu X J, Liu W C, Li A D. Optical and electrical properties study of sol-gel derived Cu_2ZnSnS_4 thin films for solar cells. AIP Advances, 2014, 4(9): 097115
34. Walter T, Herberholz R, Müller C, Schock H W. Determination of defect distributions from admittance measurements and application to $Cu(In,Ga)Se_2$ based heterojunctions. Journal of Applied Physics, 1996, 80(8): 4411–4420
35. Bube R H. Trap density determination by space-charge-limited currents. Journal of Applied Physics, 1962, 33(5): 1733–1737
36. Ritter D, Weiser K. Suppression of interference fringes in absorption measurements on thin films. Optics Communications, 1986, 57(5): 336–338
37. Urbach F. The long-wavelength edge of photographic sensitivity and of the electronic absorption of solids. Physical Review, 1953, 92 (5): 1324
38. Tumelero M A, Faccio R, Pasa A A. Unraveling the native conduction of trichalcogenides and it ideal band alignment for new photovoltaic interfaces. The Journal of Physical Chemistry C, 2016, 120(3): 1390–1399
39. Stranks S D, Eperon G E, Grancini G, Menelaou C, Alcocer M J P, Leijtens T, Herz L M, Petrozza A, Snaith H J. Electron-hole diffusion lengths exceeding 1 micrometer in an organometal trihalide perovskite absorber. Science, 2013, 342(6156): 341–344
40. Burst J M, Duenow J N, Albin D S, Colegrove E, Reese M O, Aguiar J A, Jiang C S, Patel M K, Al-Jassim M M, Kuciauskas D. CdTe solar cells with open-circuit voltage breaking the 1 V barrier. Nature Energy, 2016, 1: 16015
41. Todorov T K, Tang J, Bag S, Gunawan O, Gokmen T, Zhu Y, Mitzi D B. Beyond 11% efficiency: characteristics of state-of-the-art Cu_2ZnSn (S, Se)$_4$ solar cells. Advanced Energy Materials, 2013, 3 (1): 34–38
42. Repins I, Contreras M, Romero M, Yan Y, Metzger W, Li J, Johnston S, Egaas B, DeHart C, Scharf J, McCandless B E, Noufi R. Characterization of 19.9%-efficient CIGS absorbers. In: Proceedings of 33rd IEEE Photovoltaic Specialists Conference, 2008, 1–6
43. Jaramillo R, Sher M J, Ofori-Okai B K, Steinmann V, Yang C, Hartman K, Nelson K A, Lindenberg A M, Gordon R G, Buonassisi T. Transient terahertz photoconductivity measurements of minority-carrier lifetime in tin sulfide thin films: advanced metrology for an early stage photovoltaic material. Journal of Applied Physics, 2016, 119(3): 035101
44. Tang J, Kemp K W, Hoogland S, Jeong K S, Liu H, Levina L, Furukawa M, Wang X, Debnath R, Cha D, Chou K W, Fischer A, Amassian A, Asbury J B, Sargent E H. Colloidal-quantum-dot photovoltaics using atomic-ligand passivation. Nature Materials, 2011, 10(10): 765–771
45. Saparov B, Sun J P, Meng W, Xiao Z, Duan H S, Gunawan O, Shin D, Hill I G, Yan Y, Mitzi D B. Thin-film deposition and characterization of a Sn-deficient perovskite derivative Cs_2SnI_6. Chemistry of Materials, 2016, 28(7): 2315–2322
46. Tai K F, Gunawan O, Kuwahara M, Chen S, Mhaisalkar S G, Huan C H A, Mitzi D B. Fill factor losses in Cu_2ZnSn $(S_xSe_{1-x})_4$ solar cells: insights from physical and electrical characterization of devices and exfoliated films. Advanced Energy Materials, 2016, 6 (3): 1501609
47. Song H, Zhan X, Li D, Zhou Y, Yang B, Zeng K, Zhong J, Miao X, Tang J. Rapid thermal evaporation of Bi_2S_3 layer for thin film photovoltaics. Solar Energy Materials and Solar Cells, 2016, 146: 1–7
48. Dong Q, Fang Y, Shao Y, Mulligan P, Qiu J, Cao L, Huang J. Electron-hole diffusion lengths > 175 μm in solution-grown $CH_3NH_3PbI_3$ single crystals. Science, 2015, 347(6225): 967–970
49. Ramakrishna Reddy K T, Koteswara Reddy N, Miles R W. Photovoltaic properties of SnS based solar cells. Solar Energy Materials and Solar Cells, 2006, 90(18–19): 3041–3046
50. Kim G H, García de Arquer F P, Yoon Y J, Lan X, Liu M, Voznyy O, Jagadamma L K, Abbas A S, Yang Z, Fan F, Ip A H, Kanjanaboos P, Hoogland S, Kim J Y, Sargent E H. High-efficiency colloidal quantum dot photovoltaics via robust self-assembled monolayers. Nano Letters, 2015, 15(11): 7691–7696

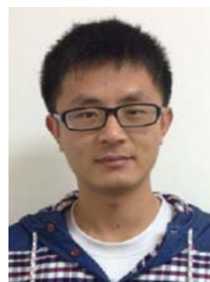

Chao Chen received the B.S. degree in School of Physics, Huazhong University of Science and Technology (HUST) China in 2014. Now, he is studying for a doctor's degree in Wuhan National Laboratory for Optoelectronics (WNLO) at HUST. He majors in photovoltaics and photodetector.

Jiang Tang received his Bachelor's degree from University of Science and Technology of China at 2003, and his Ph.D. degree in Material Science and Engineering from University of Toronto at 2010. He spent one year and half as a postdoctoral researcher at IBM T. J. Watson research center and then joined in Wuhan National Laboratory for Optoelectronics, Huazhong University of Science and Technology as a professor in 2012. His group focuses on antimony selenide (Sb_2Se_3) thin film solar cells, halide perovskites nanocrystals for light emitting and single crystals for X- and γ-ray detection. He has published 70 + papers including *Nat. Mater.*, *Nat. Photonics* with 3500 citations. He is the receiver of the "1000 Young Talents" and the National Natural Science Funds for Outstanding Young Scholar.